SCIENCE CHINA
Information Sciences

• RESEARCH PAPER •

December 2021, Vol. 64 222304:1–222304:13
https://doi.org/10.1007/s11432-019-2779-8

$\mathcal{L}$-distribution for multilook polarimetric SAR data and its application in ship detection

Tao LIU[1*], Tao TANG[1], Ziyuan YANG[1], Yanni JIANG[1],
Sheng GAO[2*] & Guangquan CHENG[3*]

[1]*School of Electronic Engineering, Naval University of Engineering, Wuhan* 430033*, China;*
[2]*College of Electrical and Information Engineering, Hunan University, Changsha* 410082*, China;*
[3]*College of System Engineering, National University of Defense Technology, Changsha* 410073*, China*

Received 21 November 2019/Revised 1 January 2020/Accepted 20 January 2020/Published online 24 November 2021

Abstract Statistical modeling based on the product model is an effective method to fit the sea clutter of polarimetric synthetic aperture radar (PolSAR) images in nonhomogeneous regions. The generalized Gamma distribution (GΓD) is a kind of distribution with wide coverage, including Weibull, Gamma, inverse Gamma, Fisher, and other distributions; it can be used as a textural variable in the product model because of its coverage and flexibility. The $\mathcal{L}$-distribution is presented to describe the statistical distribution in this product model case. The probability distribution function (PDF) of the multilook covariance matrix is obtained in the $\mathcal{L}$-distribution product model, which is presented in a closed form. Moreover, the statistics are applied to ship detection by the optimal polarimetric detector (OPD), and the analytical expressions of the probability of false alarm (PFA) and the probability of detection (PD) are both derived, which are also extended to derive the PFA of the MPWF detector. Finally, the simulated and measured data are used to verify the correctness of the theoretical derivation, and the results show that our derivations are all correct and effective.

Keywords generalized Gamma distribution (GΓD), $\mathcal{L}$-distribution, polarimetric SAR, ship detection, optimal polarization detector (OPD), multilook polarimetric whitening filter (MPWF)

Citation Liu T, Tang T, Yang Z Y, et al. $\mathcal{L}$-distribution for multilook polarimetric SAR data and its application in ship detection. Sci China Inf Sci, 2021, 64(12): 222304, https://doi.org/10.1007/s11432-019-2779-8

1 Introduction

Polarimetric synthetic aperture radar (PolSAR) has remote sensing capability with multichannel information for ocean observations and military surveillance in all-weather conditions [1]. The inshore dense ships and the situation of high sea states are two challenges in ship detection for synthetic aperture radar (SAR) images. A coupled convolutional neural network for small and densely clustered ship detection in SAR images was presented recently [2]. The sea state also affects the detection performance, which requires the different statistical models to be robust. The speckle in any coherent imagery significantly increases the difficulty of information extraction. The accuracy of the speckle model plays an important role in the interpretation of polarimetric SAR images for target detection and classification [3]. The basis of speckle suppression is the accurate acquisition of its statistical properties. In middle- and low-resolution conditions, speckles generally obey the Gaussian distribution (amplitude Rayleigh distribution) that satisfies the central limit theorem [4, 5]. With the increasing resolution of modern radars, radar echoes with a small number of scatterers or significant scatterers in a resolution cell tend to have long-tailed characteristics. Therefore, radar echoes no longer obey the Gaussian distribution, and non-Gaussian statistical models are needed to characterize the statistical properties of sea clutter. Non-Gaussian distributions, such as the Gamma distribution, inverse Gamma distribution, lognormal distribution, and the Weibull distribution, are often used to describe the scattering characteristics of such nonhomogeneous clutter [6, 7]. These four distributions can be regarded as special cases of the generalized Gamma distribution functions

* Corresponding author (email: liutao1018@sina.com, gaosh8899@126.com, cgq299@163.com)

(GΓD). In addition, it is worth noting that an excellent $\mathcal{G}_{\rm AO}$ model was recently proposed in [8]. The good performance of this model for characterizing nonhomogeneous clutter was also demonstrated. Li et al. [9] proposed a statistical model of SAR based on the generalized Gamma distribution. The model has strong adaptability but there is no closed analytical expression and it cannot do multilook data processing. Another kind of non-Gaussian distribution is a multivariate product model. Owing to its clear physical mechanism and robust full-polarization processing capability in PolSAR information processing, the multivariate product model has been widely used in modeling, signal processing, and data analysis for long-tailed clutter [10]. The model shows that the radar cross section (RCS) is equivalent to the product of the coherent speckle and the texture component [10]. The $\mathcal{K}$ and $\mathcal{G}_0$ product models are widely used for nonhomogeneous sea clutter. If an inverse Gaussian distribution is regarded as a texture component in complex inhomogeneous regions, the accordant product model $\mathcal{G}$ has been proven to have good fitting accuracy with a closed analytical expression [11]. The $\mathcal{G}$ distribution covers many kinds of distributions but the corresponding parameter estimation is complicated. If the GΓD is used as the textual variable, the product model will have an $\mathcal{L}$-distribution, which was proposed by us in 2014 [10]. Song et al. [12] used the general Fisher distribution (G$\mathcal{F}$D) to model the texture and it is clear that the G$\mathcal{F}$D's coverage is smaller than that of the GΓD distribution. Other researchers have begun to study the $\mathcal{L}$-distribution since it covers more areas and is more flexible than the $\mathcal{G}$ distribution in the log-cumulants plane [13]. However, there is still no closed-form expression of the probability density function (PDF). Therefore, it is necessary to study GΓD distribution and try to obtain the analytical expressions of the corresponding PDF and probability of false alarms (PFA).

The $\mathcal{L}$-distribution model can be applied to ship detection. There are three ways to perform ship detection. The first is the target decomposition, the second is the ship wake, and the last is the optimal techniques. In SAR images, backscattering from ships is usually brighter than that from the sea background, which can be applied to detect ships by a statistical test on the intensity of both ships and sea clutter [14]. Novak et al. [15, 16] proposed an optimal polarimetric detector (OPD) based on the likelihood ratio test (LRT) when the statistics of ships and clutter are both known, which belongs to optimal techniques. In the same assumption, the theory of target decomposition can also be used to improve detection performance via different physical characteristics of ships and clutter. Unfortunately, it is quite difficult to derive the statistics of ship backscattering because it mainly relies on the physical characteristics of ships themselves. When ships to be detected are very small, ship wakes may be used to detect them. However, many factors, such as angle of view and angle of incidence, radar frequency, and sea state, will influence the ship wakes, which leads to the unreliability of ship wakes. Therefore, in ship detection, the constant false alarm rate (CFAR) tests are generally used, which select the threshold via the sea clutter statistics to keep PFA constant locally [1]. Recently, Marino et al. [14] proposed a polarimetric notch filter (PNF) when the ship statistics are unknown, which separates ships and sea clutter based on their polarimetric characteristics. In fact, the polarimetric whitening filter (PWF) can also work in the absence of prior information, which has been proved to be able to improve the ship detection performance, though it has been presented for many years [16, 17]. The PWF can minimize the speckle variation owing to the polarimetric information of sea clutter. It is well known that the performance of PWF was comparable with that of the OPD [16, 17]. Liu et al. [18, 19] developed the PWF to the multilook polarimetric whitening filter (MPWF). The expressions of the probability of false alarms (PFAs) and the detection threshold of the MPWF have been derived recently [19], while the PFA and the threshold of the OPD are still unknown.

The structure of this paper is organized as follows. Firstly, the product model is introduced, followed by the GΓD distribution and the $\mathcal{L}$-distribution. The PDF of the $\mathcal{L}$-distribution is presented in a closed form. Secondly, the approximate expression of the PFA of the $\mathcal{L}$-distribution is derived and applied to ship detection by the OPD method. Finally, the simulated data and real data are used to validate correctness and robustness of the OPD detector compared with other detectors which are used widely. The results of tests verify our derivation and the performance of the detectors meets our expectation.

2 Proposed $\mathcal{L}$-Wishart model

2.1 Multivariate product model

The backscattering statistics of an SAR image is usually fluctuated. The fluctuation is always affected by two factors. One is the interference between scatterers within a resolution cell, which is named speckle.

The other factor is the RCS, which is called as texture. When the speckle is fully developed, the texture can be seen as constant, and the PDF of the polarimetric covariance matrix can be characterized by a Wishart distribution. If the texture is varied, the statistics of clutter can be modeled by a multivariate product model by two independent variables. The polarimetric scattering vector in the product model can be expressed as follows [16]:

$$\boldsymbol{w} = \sqrt{\tau}\boldsymbol{y}, \tag{1}$$

where τ is the texture variable which is scaled, and $\boldsymbol{y}$ is the speckle vector which is distributed as a zero-mean multivariate complex-Gaussian distribution. Generally speaking, the fluctuation of texture is varied slower than speckle, and therefore the texture in each polarization channel is assumed to be the same. The multilook covariance matrix is defined as [16]

$$\boldsymbol{C} = \frac{1}{L}\sum_{i=1}^{L}\boldsymbol{w}_i\boldsymbol{w}_i^{\mathrm{H}} = \frac{1}{L}\sum_{i=1}^{L}\tau_i\boldsymbol{y}_i\boldsymbol{y}_i^{\mathrm{H}}, \tag{2}$$

where the subscript H is the conjunction transform and L is the number of looks, and τ_i is independent of i. Then, Eq. (2) can be written as [16, 20]

$$\boldsymbol{C} = \tau\boldsymbol{Y}, \tag{3}$$

where $\boldsymbol{Y}$ is a random matrix only affected by speckle. Therefore, $\boldsymbol{Y}$ obeys the Wishart distribution.

Since the texture and speckle are independent, they can be obtained [20] by

$$\boldsymbol{\Sigma} = \mathrm{E}\left\{\boldsymbol{C}\right\} = \mathrm{E}\left\{\tau\right\}\mathrm{E}\left\{\boldsymbol{Y}\right\} = \mathrm{E}\left\{\tau\right\}\Gamma, \tag{4}$$

where $\Gamma = \mathrm{E}\{\boldsymbol{y}\boldsymbol{y}^{\mathrm{H}}\}$ is the covariance matrix of the speckle in the Gaussian case, $\boldsymbol{\Sigma}$ is the statistical mean of the covariance matrix $\boldsymbol{C}$, and E is the mathematical expectation operator.

The multivariate product model consists of a texture variable and a complex Gaussian vector which are independent of each other. The key to modeling the PolSAR image data by the product model is the selection of the statistical model for texture components. The GΓD distribution is a flexible model that involves many kinds of distributions, including the Rayleigh distribution, Weibull distribution, Gamma distribution, inverse Gaussian distribution, and the square root Gamma distribution.

The texture obeying the GΓD distribution means that the PDF of its intensity satisfies the following form (the amplitude distribution is also obeyed the GΓD distribution [9]):

$$\tau \sim f(\tau; k, v) = \frac{|v|\,k^k}{\sigma\Gamma(k)}\left(\frac{\tau}{\sigma}\right)^{kv-1}\exp\left\{-k\left(\frac{\tau}{\sigma}\right)^{v}\right\}, \tag{5}$$

where $\Gamma(\cdot)$ is a Gamma function and σ, k, v are the scale, shape and power parameters of the GΓD distribution, respectively. When $\sigma = k^{1/v}\Gamma(k)/\Gamma(k+1/v)$, the mean of τ is the unit. In the product model, the texture variable is always scaled. When $v = -1$, the GΓD distribution is simplified to be an inverse Gamma distribution. When $k = 1$, the GΓD distribution is simplified to the Weibull distribution, and when $v = 1$, the GΓD distribution is simplified to a Gamma distribution. It should be pointed out that when $v = 0$, the corresponding GΓD distribution is characterized as a lognormal distribution.

2.2 Distribution of the $\mathcal{L}$-Wishart model

The complex Gaussian vector $\boldsymbol{y}$ in (1) obeys the Gaussian distribution [21]:

$$f_{\boldsymbol{y}}(\boldsymbol{y}) = \frac{1}{\pi^d\left|\boldsymbol{C}\right|}\exp\left(-\boldsymbol{y}\boldsymbol{C}^{-1}\boldsymbol{y}^{\mathrm{H}}\right), \tag{6}$$

where d is the dimension of the complex Gaussian vector and $|\cdot|$ is the determinant operator. The corresponding multilook covariance matrix is $\boldsymbol{Y}$, which obeys the Wishart distribution [21]:

$$f_Y(\boldsymbol{Y}) = \frac{L^{Ld}|\boldsymbol{Y}|^{L-d}\exp(-L\mathrm{Tr}(\Gamma^{-\mathbf{1}}\boldsymbol{Y}))}{\Gamma_{\mathrm{d}}(L)|\Gamma|^{L}}, \tag{7}$$

where $\Gamma = \mathrm{E}(\boldsymbol{y}\boldsymbol{y}^{\mathrm{H}})$. $\Gamma(\cdot)$ is the Gamma function and $\Gamma_{\mathrm{d}}(L)$ is

$$\Gamma_{\mathrm{d}}(L) = \pi^{\frac{1}{2}d(d-1)}\Gamma(L)\cdots\Gamma(L-d+1). \tag{8}$$

When the texture variable obeys a GΓD distribution, the probability density function (PDF) of the $\mathcal{L}$-distribution covariance matrix is easily obtained [10] as follows:

$$f_{\boldsymbol{Z}_C^{(L)}}(\boldsymbol{Z}) = \frac{\eta^{Ld}|\boldsymbol{Z}|^{L-d}}{\Gamma_{\mathrm{d}}(L)|\boldsymbol{C}|^{L}\Gamma(k)}\mathcal{L}\left(v, kv - Ld, \eta\mathrm{Tr}(\boldsymbol{C}^{-1}\boldsymbol{Z})\right), \tag{9}$$

where

$$\begin{aligned}\mathcal{L}(a,b,z) &= 2\,|a|\int_0^{\infty} t^{2b-1}\exp\left(-t^{2a} - zt^{-2}\right)\mathrm{d}t = |a|\int_0^{\infty} x^{b-1}\exp\left(-x^{a} - \frac{z}{x}\right)\mathrm{d}x \\ &= \begin{cases} H_{0,2}^{2,0}\left[z\,\middle|\,\begin{matrix} \\ (0,1),(\frac{b}{a},\frac{1}{a})\end{matrix}\right], & a>0, \\ H_{1,1}^{1,1}\left[z\,\middle|\,\begin{matrix}(1-\frac{b}{a},-\frac{1}{a}) \\ (0,1)\end{matrix}\right], & a<0,\end{cases}\end{aligned}$$

$\eta = \frac{Lk^{1/v}}{\sigma} = \frac{L\Gamma(k+1/v)}{\Gamma(k)}$, and $H(\cdot)$ is the Fox H-function which defined as [22]

$$H_{p,q}^{m,n}\left[z\,\middle|\,\begin{matrix}(a_i,A_i)_{1,p} \\ (b_j,B_j)_{1,q}\end{matrix}\right] = \frac{1}{2\pi i}\int_{\Theta}\frac{\prod_{j=1}^{m}\Gamma(b_j+B_js)\prod_{j=1}^{n}\Gamma(1-a_j-A_is)}{\prod_{j=n+1}^{p}\Gamma(a_j+A_is)\prod_{j=m+1}^{q}\Gamma(1-b_j-B_js)}z^{-s}\mathrm{d}s, \tag{10}$$

where $z, c, a_i, b_j \in C$, $A_i, B_j \in \mathbb{R}^{+}$ and $m,n,p,q \in \mathbb{Z}$, such that $1 \leqslant j \leqslant m, 1 \leqslant i \leqslant n$, $0 \leqslant m \leqslant q, o \leqslant n \leqslant p$, $A_i > 0, B_j > 0$. Θ is a contour in the complex s-plane ranging from $\varsigma - i\infty$ to $\varsigma + i\infty$. In [10,11], $\mathcal{L}(a,b,z)$ is only presented in an integral form. Here, we obtain a closed form, which is a development of $\mathcal{L}(a,b,z)$. The Fox H-function with MATLAB code can be found in [23].

3 Statistics of the OPD in ship detection

The OPD put forward by Novak processes the complete polarization scattering matrix (PSM) and provides the best possible detection performance from polarimetric radar data [15]. The quadratic form of OPD is

$$z = \mathrm{tr}\left[\left(\boldsymbol{\Sigma}_C^{-1} - \boldsymbol{\Sigma}_T^{-1}\right)\boldsymbol{Z}\right] \underset{\text{clutter}}{\overset{\text{target}}{\gtrless}} T, \tag{11}$$

where $\mathrm{tr}(\cdot)$ is the trace operator and $\boldsymbol{\Sigma}_C$ and $\boldsymbol{\Sigma}_T$ are the polarimetric covariance matrices of clutter and targets, respectively. $\boldsymbol{Z}$ is the multilook covariance matrix, and T is the detection threshold. If $z > T$, it is detected as a target, otherwise as clutter. The sensitivity of the OPD detector was analyzed in previous literatures under the Wishart and $\mathcal{K}$-Wishart distribution cases; however, the expression is very complicated and requires much computational time [15]. The PFA or probability of detection (PD) of the OPD in the $\mathcal{L}$-distribution can also be derived by following the steps in the $\mathcal{K}$-distribution case [15]; however, its calculation is also very complicated. Therefore, the approximation is given in this section, which is simpler and more easily calculated in practical applications.

3.1 Approximation of statistics in the $\mathcal{L}$-Wishart model

In measured polarimetric images, a real PDF of the OPD is only approximated by a quadratic form rather than equaling a quadratic form since the data would not completely obey the hypothesis. Therefore many approximations have been proposed. The PDF and PFA of OPD algorithm can be derived in Appendix.

$$P_{\mathrm{fa}/d} = 1 - \frac{T}{\Gamma(Lb)\Gamma(k)}\left(\frac{k^{1/v}L}{a\sigma}\right)\begin{cases} H_{1,3}^{2,1}\left[\frac{k^{1/v}LT}{a\sigma}\,\middle|\,\begin{matrix}(0,1) \\ (Lb-1,1),(\frac{kv-1}{v},\frac{1}{v}),(-1,1)\end{matrix}\right], & v>0, \\ H_{2,2}^{1,2}\left[\frac{k^{1/v}LT}{a\sigma}\,\middle|\,\begin{matrix}(0,1),(1-k+\frac{1}{v},-\frac{1}{v}) \\ (Lb-1,1),(-1,1)\end{matrix}\right], & v<0.\end{cases} \tag{12}$$

We can also obtain the threshold of the detection via a bisection method when the PFA is constant, which is called constant false alarm rate (CFAR) processing.

3.2 Extension of the PFA to the MPWF

The output after the polarimetric whitening filter (PWF) in PolSAR imagery is defined as follows [20]:

$$z_{\mathrm{MPWF}} = \frac{1}{L}\sum_{i=1}^{L} \boldsymbol{w}_i{}^{\mathrm{H}} \boldsymbol{\Sigma}_C^{-1} \boldsymbol{w}_i = \operatorname{tr}\left(\boldsymbol{\Sigma}_C^{-1}\boldsymbol{C}\right) = \tau \operatorname{tr}\left(\boldsymbol{\Sigma}_C^{-1}\boldsymbol{Y}\right) = \tau z_{\mathrm{YPWF}}. \tag{13}$$

The variable z_{YPWF} accurately obeys a Gamma distribution [20], that is, $z_{\mathrm{YPWF}} \sim \gamma\left(Ld, \frac{1}{L}\right)$, which is a special case of (12) when $b = d; a = 1$. Then, we can obtain the PFA of MPWF from (13) under the $\mathcal{L}$-distribution hypothesis,

$$P_{\mathrm{fa}} = 1 - \frac{T}{\Gamma(Ld)\Gamma(k)}\left(\frac{k^{1/v}L}{\sigma}\right)\begin{cases} H_{1,3}^{2,1}\left[\frac{k^{1/v}LT}{\sigma}\middle| \begin{matrix}(0,1)\\ (Ld-1,1),(\frac{kv-1}{v},\frac{1}{v})(-1,1)\end{matrix}\right], & v>0,\\ H_{2,2}^{1,2}\left[\frac{k^{1/v}LT}{\sigma}\middle| \begin{matrix}(0,1),(1-k+\frac{1}{v},-\frac{1}{v})\\ (Ld-1,1),(-1,1)\end{matrix}\right], & v<0.\end{cases} \tag{14}$$

Eq. (13) is a special case of (12), which has the same form as that in [19].

4 Experimental validation and ship detection

4.1 Numerical derivation validation

The simulated SAR data in the product model is generated through Monte Carlo simulation. In the simulation, we generate the Wishart distribution covariance matrix and the textual variable respectively.

There are 1000000 covariance matrix samples in the synthetic dataset, which obey a complex Wishart distribution with zero mean. The covariance matrix of Wishart distribution is produced by averaging a homogeneous region of the measured SAR data, which makes the simulation reliable. The textual variable was simulated according to the statistical parameters in (5). The texture component of the proposed $\mathcal{L}$ distribution obeys the generalized Gamma distribution, which can be generated by the sum of squares from Gaussian random variables. The number of looks was set to $L = 10$. The simulated results are presented in Figure 1, which show that the simulated data are well consistent with the theoretical results. The results also show that the approximations can accurately fit the hypothesis model.

The performances of different detectors are also presented here via simulation, such as multilook MPMF, OPCE, MPWF, PNF and multilook optimal polarimetric detector (MOPD). The receiver operation characteristic (ROC) curves are presented in Figure 2 when the target to clutter ratio (TCR) is constant. In simulation experiments, we need to change the TCR freely to study the detection performance more comprehensively, where $\mathrm{TCR} = \operatorname{tr}(\boldsymbol{\Sigma}_T - \boldsymbol{\Sigma}_C)/\operatorname{tr}(\boldsymbol{\Sigma}_C)$ [15]. In Figure 2 the OPCE is overlapped with the MPMF, which shows they have the same performance. The OPD has a little better performance than MPWF, and the MPMF performs well when the TCR is big enough. The PNF gives the worst performance in our simulation. Here the P_{fa} is the probability of false alarm, and P_{d} is the probability of detection.

4.2 Ship detection results of real data

(i) Flow of the OPD algorithm in practice. In practical applications, the ship characteristics are generally unknown, which leads the OPD method to be a theoretical analysis tool but of no use in practical applications. We want to change this and make the OPD more applicable. The problem is how to obtain the covariance matrix of the ship target. Since the MPWF can obtain the closest performance compared with the OPD, it is reasonable to obtain the ship characteristics by the results of the MPWF. At the same time, we cannot obtain the accurate covariance matrix of each ship, and we use the average covariance matrix of all ships as the ship characteristics. Therefore, we design an OPD flow of CFAR processing as shown in Figure 3. The dotted line is the MPWF progress, and the full line is the OPD progress. The diamond is the decision of the termination of the iterative estimation of MPWF. The statistics of both

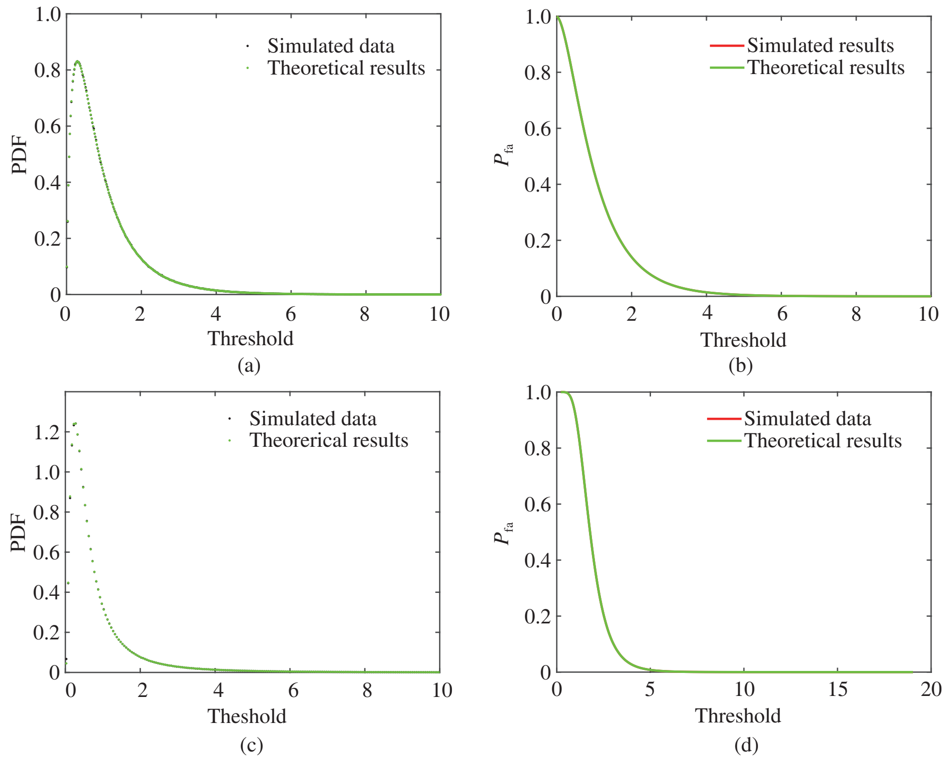

Figure 1 (Color online) PDF/PFA of the OPD for different parameter v. PDF of the OPD when (a) $v>0$, (b) $v<0$; PFA of the OPD when (b) $v>0$ and (d) $v<0$.

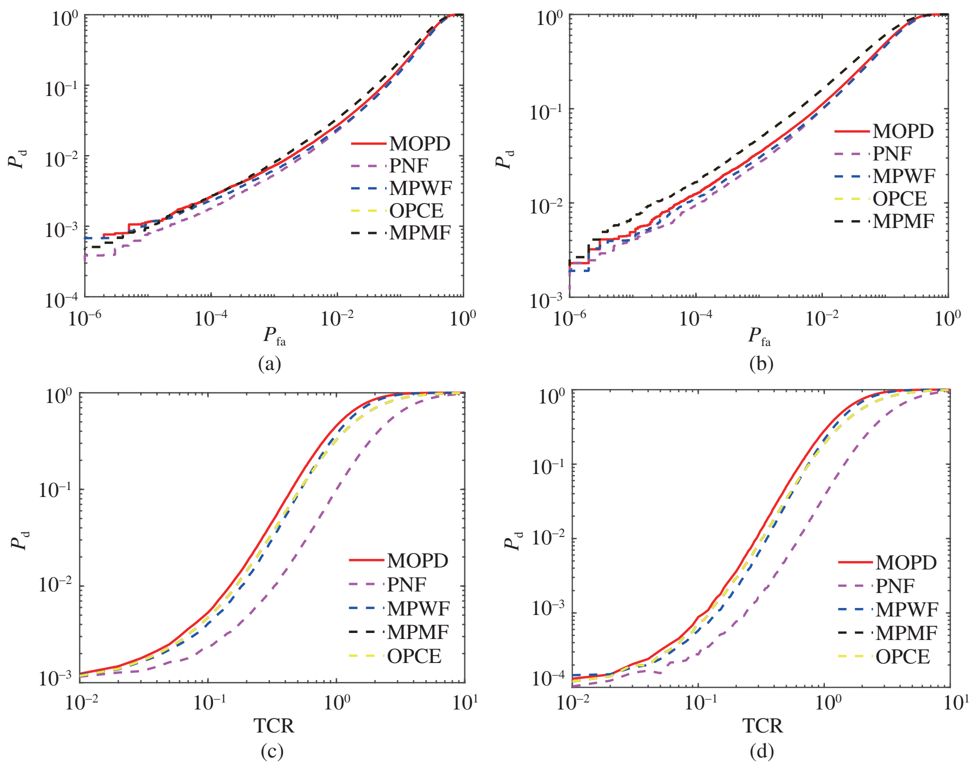

Figure 2 (Color online) Performances of different detectors in different TCR and PFA cases. (a) TCR = 0.5; (b) TCR = 2; (c) $P_{\rm fa}$ = 1E−3; (d) $P_{\rm fa}$ = 1E−4.

targets and sea clutter are estimated by repetitions for high accuracy. The fast block CFAR detector is used here [24]. The steps are improved as follows:

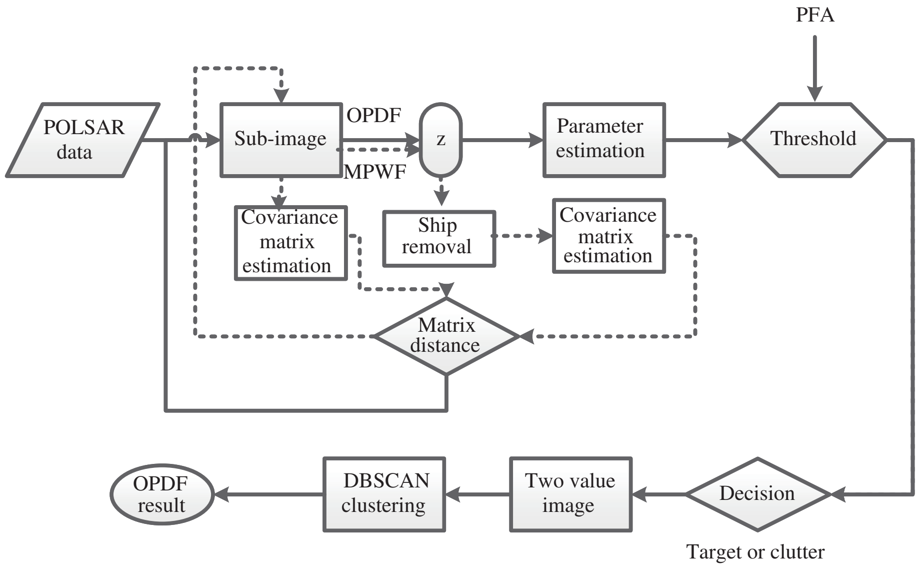

Figure 3 OPD flow chart of CFAR processing.

Step 1. Divide the whole PolSAR image into equal-sized blocks (here we take the size of the block as 66×66, estimate the covariance matrix, and perform the MPWF processing.

Step 2. Determine a simple threshold of approximately 25 to remove the bright outliers by this threshold, and then update the estimation of the polarimetric covariance matrix.

Step 3. MPWF will be operated several times until the difference (distance) of the covariance matrix is small enough under a fixed threshold. Two or three repetitions are generally sufficient. Then we get the clutter information together with ships.

Step 4. Estimate the parameters of the statistical model of each block by the log-cumulants method. Use the bisection method to obtain the threshold for the MPWF image via (12) and (14). Then we can determine whether the pixel is a ship or clutter.

Step 5. Delete the solo points by DBSCAN (density-based spatial clustering of applications with noise) method with $\varepsilon = 10$ and MinPt $= 2$ [25].

Step 6. Via the ship characteristics derived in Step 6, we perform the CFAR processing of OPD, which is shown by the dotted line in Figure 3.

Step 7. Combine the results of the sub-images, and the final detection image is derived.

The flow chart of the OPD is presented as follows.

In addition, the threshold in step 2 affects the results of parameter estimation surely. The threshold cannot be too small, otherwise it can generate a large bias of the parameters; and it cannot be too large, otherwise it will include many ship pixels and make the detection threshold higher. The simple threshold is set to 25, and it is also proven to be reasonable by the measured experiments in parts (iii)–(v).

(ii) Parameter estimation of the sea clutter and targets. The outstanding performance of the Mellin transform in the field of SAR image parameter estimation has attracted the interest of many researchers [26, 27]. A new parameter estimation method based on the Mellin transform (log-cumulants) of the polarimetric covariance matrix has been proposed [28, 29]. Traditionally, the second and third log-cumulants of the multilook covariance matrix are used for parameter estimation in product models. The estimators via log-cumulants on the MPWF were proposed [30] in both $\mathcal{K}$ and $\mathcal{G}_0$ distribution cases. Recently, a novel method based on log-cumulants and the MPWF has been proposed to improve the estimation accuracy, with excellent effect [30]. Therefore, the estimation of the $\mathcal{L}$- distribution model is performed by combining the log-cumulants and MPWF.

(iii) The measured dataset from NASA/JPL AIRSAR DATA. The real data comes from a polarimetric dataset of NASA/JPL AIRSAR with 9-look, which covers an area close to Tamano City, Japan. The data set is collected from the AIRSAR instrument of the DC-8 aircraft during the PACRIM-2 task on 4 October 2000, which consists of the full-polarization data. The range pixel resolution is 3.3 m, and the azimuth pixel resolution is 4.6 m. The details of the PolSAR system parameters can be found in [31]. The dataset is formatted in the Stokes matrix originally. Lately, they are converted to the covariance matrix of the PolSAR data for ship detection. We select two sub-images of the same area with different

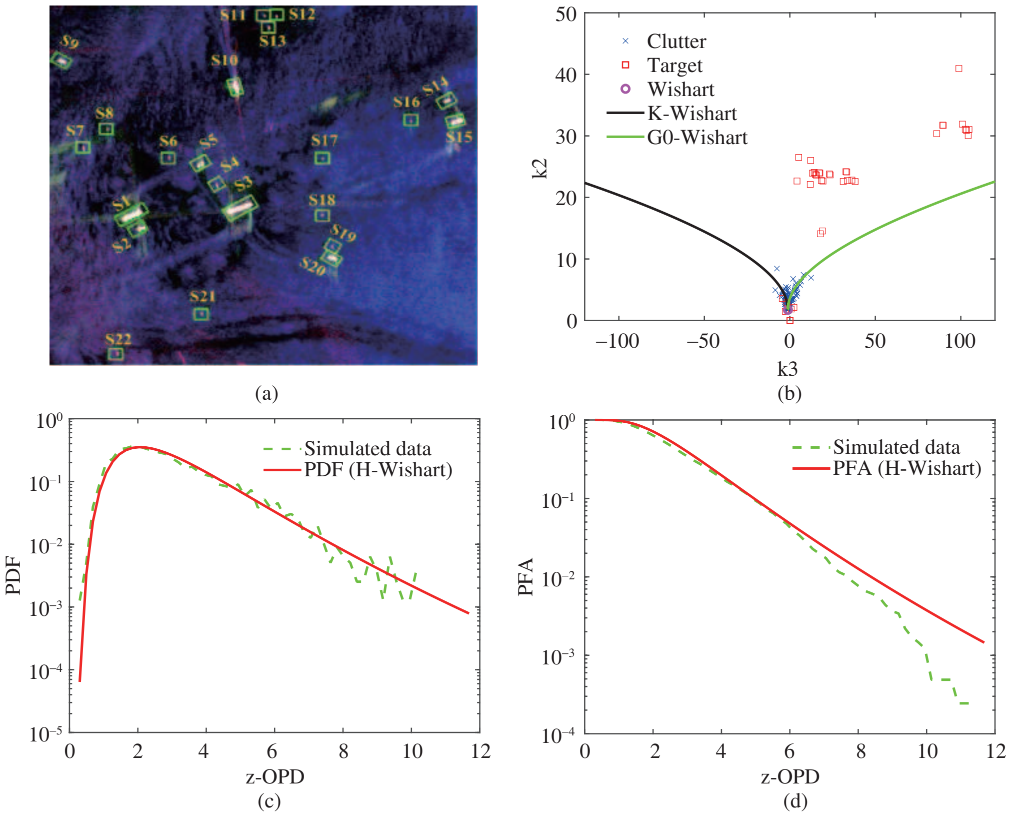

Figure 4 (Color online) Measured data and the GOF of the statistical model in L-Band. (a) Measured data in Kojimawan in L-Band [31]; (b) diversity diagram of the k2k3 plane; (c) PDF; (d) PFA.

bands to validate the effectiveness of the proposed CFAR algorithm. The size of the area is 768×691 (Samples $\times$ Lines) (see Figures 4 and 6).

(iv) Ship detection in the L-Band image. Since there are two kinds of datasets including both L-Band polarimetric SAR data and C-Band polarimetric SAR data, it is a good idea to analyze the detection performance among different detectors on both images. The ground-truth of the ROI is presented in Figure 4 by visual inspection combining both the L-Band image and the C-band image. There are 22 ships in this area. The statistical models are presented in the log-cumulants plane [29, 32] in Figure 4(b). Here the targets presented as red rectangles are the outliers removed by the simple threshold in Step 2. The H-Wishart distribution is used to model the clutter. The goodness of fit of a random block data is listed in Figures 4(c) and (d). The KL distance [33] is used to measure the goodness-of-fit. The average of the KL distance is 0.01, which shows that the H-Wishart distribution can fit the statistical model accurately.

Since the polarimetric characteristics of ships are hard to be derived, we use the average of the ship covariance matrices. In addition, a figure of merit (FOM) is used to evaluate the detection performance [31],

$$\mathrm{FOM} = \frac{N_{\mathrm{td}}}{(N_{\mathrm{fa}} + N_{\mathrm{gt}})}, \tag{15}$$

where N_{td} is the number of detected ships, N_{fa} is the number of false ships, N_{gt} is the number of real ships. In the following figures a red rectangle means an omitted target, a yellow rectangle means a false target, and a green rectangle means one true ship. $\hat{P}_{\mathrm{fa}}$ means the actual false alarm, and the value in the bracket is the number of isolated pixels. The detection results are presented in Figure 5 and Table 1.

The detection results of different detectors are both listed in Figure 5. The yellow rectangle means false alarm. It can be seen from Figure 5(a) that the MPWF detector generates 4 false alarms and that all the ships are detected. The OPD detector also generates 4 false alarms and exhibits a similar performance compared with the MPWF. From Figure 5 and Table 1, the PNF gives the worst performance according to the FOM, and the maintenance of the CFAR is not good. The MPMF is also worse than the MPWF and MOPD.

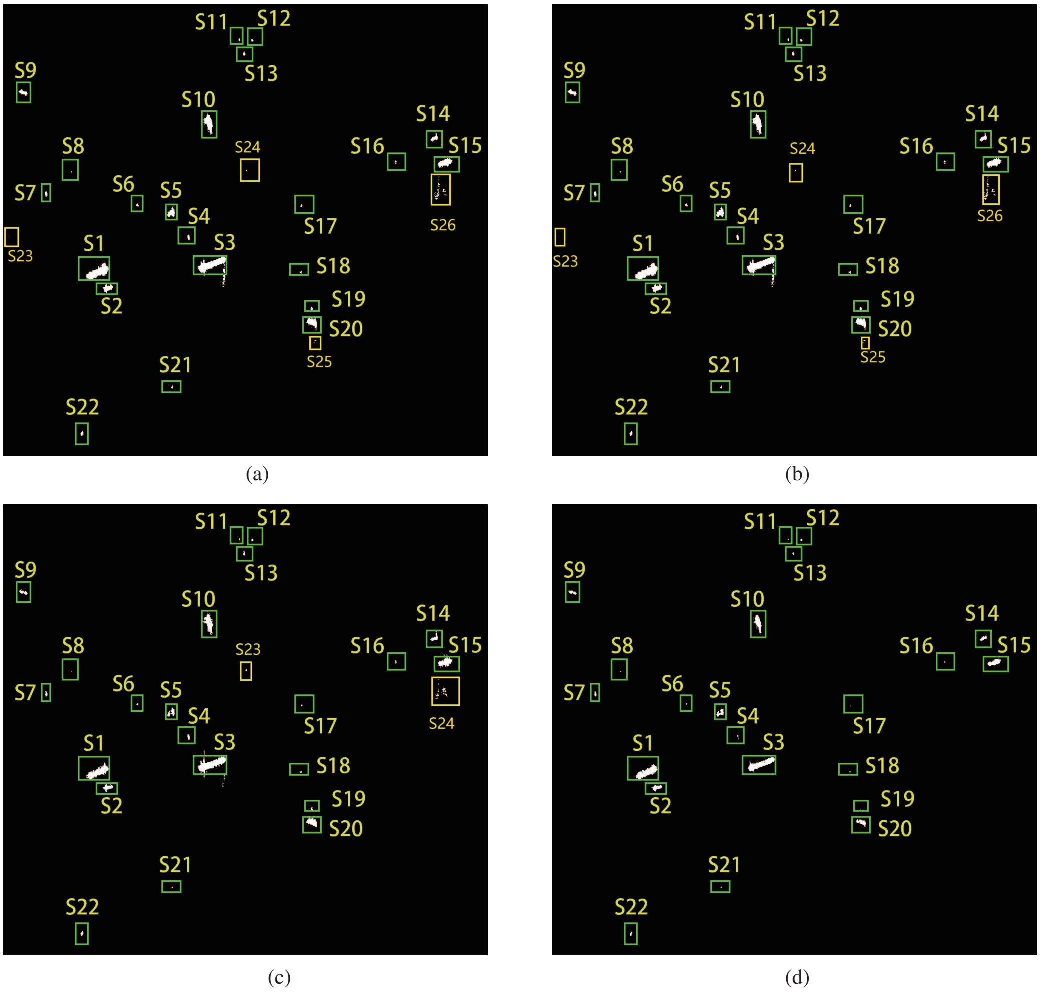

Figure 5 (Color online) Detection results of diffrent detectors when CFAR = 1E−5 in L-Band. (a) MPWF; (b) OPD; (c) MPMF; (d) PNF.

Table 1 Pixel numbers of different ships in different detectors when CFAR = 1E−5

Band	Method	$\hat{P}_{\mathrm{fa}}$	N_{td}	N_{fa}	FOM (%)
L	PNF	3.3E−6 (20)	22	0	52.38
	MPMF	2.0E−5 (12)	22	2	61.11
	MPWF	1.1E−5 (7)	22	4	66.67
	MOPD	1.0E−5 (6)	22	4	68.75

(v) Ship detection in the C-Band image. The Pauli image of C-Band is listed in Figure 6, and the k2-k3 log-cumulants are also presented. In Figure 6(a) there are many ghosts. The H-Wishart distribution is used to model the clutter. The average of the KL distances is also 0.01, which also shows that the H-Wishart distribution can model the statistics accurately.

In C-band measured images, azimuth ambiguities of the strong scatters usually cause false targets [34], which are also called ghosts. As is shown in Figure 6(a) with 12 purple rectangles (G1–G11). In fact because the phase difference between the ambiguities of the HV and VH components of a calibrated single look complex (SLC) image is approximately π and their magnitudes are approximately equal [34], the scattering properties of S_{HV} and S_{VH} are used to obtain an image without ambiguity to detect ships in [34]. Since we only have the multilook complex data (MLC) instead of the SLC data, we can use the item of cross-polarimetric MLC components HV + VH (C_{HV}) to remove this ambiguity after the MPWF or MOPD. Since the aim of this experiment is to get the performances of different detectors, we do not use this method to remove the ambiguity. This pre-processing changes the statistical model of the sea clutter, which should be studied to construct a new detection algorithm in future. We can assume

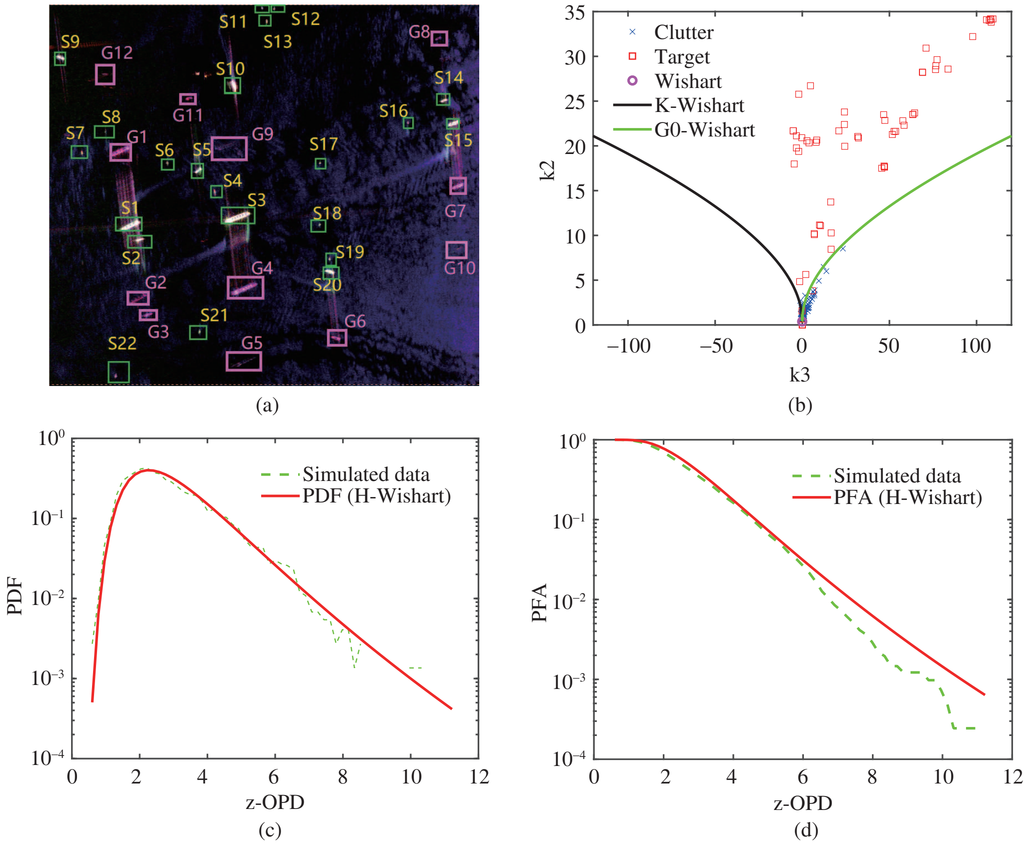

Figure 6 (Color online) Measured data and the GOF of the statistical model in C-Band. (a) Measured data in Kojimawan in C-Band; (b) diversity diagram of the k2-k3 plane; (c) PDF; (d) PFA.

Table 2 Pixel numbers of different ships in different detectors when CFAR = 1E−5

Band	Method	$\hat{P}_{\mathrm{fa}}$	N_{td}	N_{fa}	FOM (%)
C	PNF	4.5E−5 (27)	22	8	38.60
	MPMF	5.3E−5 (32)	21	11	32.31
	MPWF	1.0E−5 (6)	21	5	63.64
	MOPD	1.0E−5 (6)	21	5	63.64

that the ghosts have been removed in the performance evaluation. The detection results are presented in Figure 7 and Table 2. A red rectangle is denoted as an omitted target.

In C-Band image, we can see the maintenances of CFAR are held stably in MOPD and MPWF according to our set. The FOMs of MPWF and MOPD are the highest. There is one target omitted except that in the PNF image. Overall, the maintenances of CFAR can keep the best both in the L-Band image and in the C-Band image. The results in the C-Band images are almost the same with those in the L-Band images.

5 Conclusion

In this paper, the closed-form expression of the statistical model was derived in the product model with GGD distribution as texture. The analytical expressions of PD/PFA were also derived for the OPD, and extended to the MPWF. Moreover, they are applied to ship detection. The CFAR flow of the OPD under the condition that the scattering characteristics of targets are unknown was constructed with the help of the detection results of the MPWF, which exhibits a new idea for the application of the OPD in practice. Since the ship characteristics are difficult to be obtained, the average of the polarimetric covariance matrix is used in the OPD, which leads to little improvement compared with the MPWF. In fact, many other mechanisms that remain in ship detection, such as polarization decomposition and ship

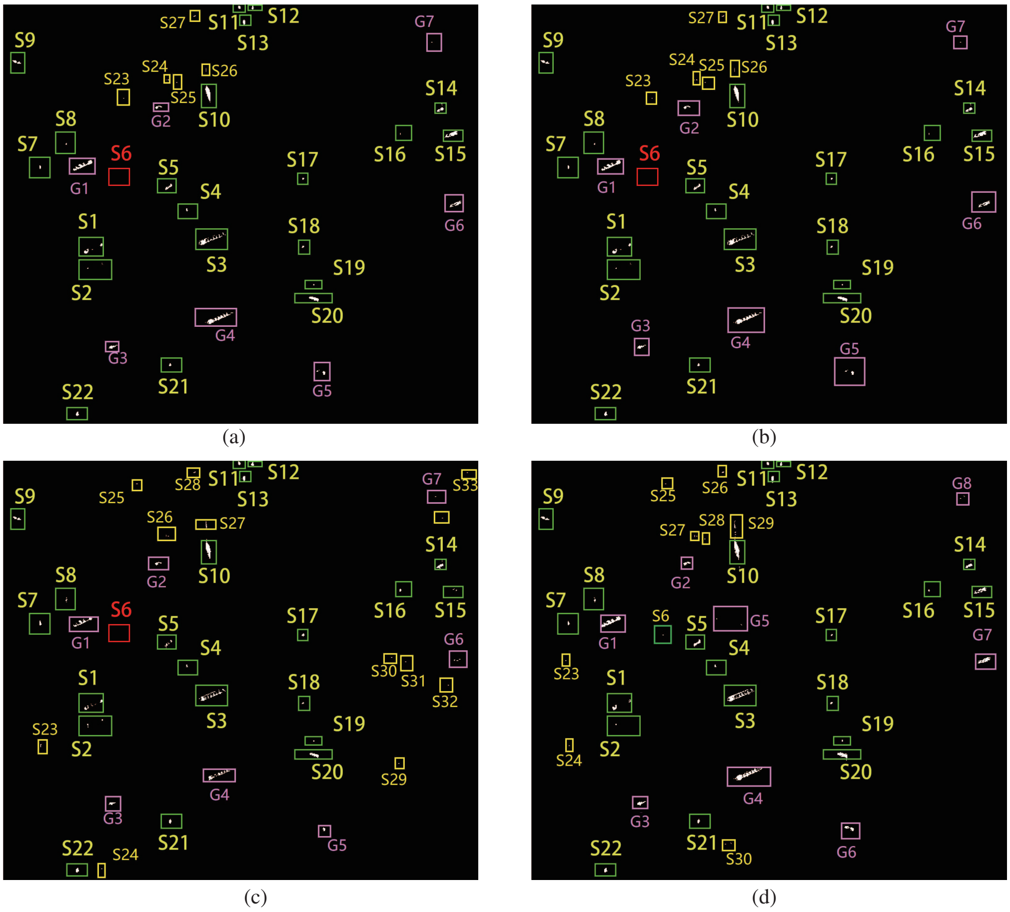

Figure 7 (Color online) Detection results of different detectors when CFAR = 1E−5 in C-Band. (a) MPWF; (b) OPD; (c) MPMF; (d) PNF.

wake, may be more useful for small ships. In future work, we will study ship wake detection to detect small targets.

Acknowledgements This work was supported in part by National Natural Science Foundation of China (Grant Nos. 61771483, 41822105, 61490693), Key Research Plan of Hunan Province (Grant No. 2019SK2173), Field Foundation (Grant No. 61404160109), and Fundamental Research Funds for the Central Universities (Grant No. 2682020ZT34).

References

1 Tao D, Anfinsen S N, Brekke C. Robust CFAR detector based on truncated statistics in multiple-target situations. IEEE Trans Geosci Remote Sens, 2016, 54: 117–134
2 Zhao J P, Guo W W, Zhang Z H, et al. A coupled convolutional neural network for small and densely clustered ship detection in SAR images. Sci China Inf Sci, 2019, 62: 042301
3 Bouhlel N, Meric S. Maximum-likelihood parameter estimation of the product model for multilook polarimetric SAR data. IEEE Trans Geosci Remote Sens, 2019, 57: 1596–1611
4 Liu T, Huang G M, Wang X S, et al. Statistical assessment of H/A target decomposition theorems in radar polarimetry. Sci China Inf Sci, 2010, 53: 355–366
5 Liu T, Cui H G, Xi Z M, et al. Novel estimators of equivalent number of looks in polarimetric SAR imagery based on sub-matrices. Sci China Inf Sci, 2016, 59: 062309
6 Deng X, López-Martínez C, Chen J, et al. Statistical modeling of polarimetric SAR data: a survey and challenges. Remote Sens, 2017, 9: 348
7 Liu T, Huang G-M, Wang X-S, et al. Statistics of the polarimetric weibull-distributed electromagnetic wave. IEEE Trans Antenn Propagat, 2009, 57: 3232–3248
8 Gao G, Gao S, Ouyang K, et al. Scheme for characterizing clutter statistics in SAR amplitude images by combining two parametric models. IEEE Trans Geosci Remote Sens, 2018, 56: 5636–5646
9 Li H-C, Hong W, Wu Y-R, et al. On the empirical-statistical modeling of SAR images with generalized Gamma distribution. IEEE J Sel Top Signal Process, 2011, 5: 386–397
10 Liu T, Cui H G, Xi Z M, et al. Modeling polarimetric SAR images with L-distribution and novel parameter estimation method (in Chinese). Sci Sin Inform, 2014, 44: 1004–1020
11 Khan S, Guida R. Application of Mellin-kind statistics to polarimetric distribution for SAR data. IEEE Trans Geosci Remote Sens, 2014, 52: 3513–3528
12 Song W Y, Li M, Zhang P, et al. The WG distribution for multilook polarimetric SAR data and its application. IEEE Geosci Remote Sens Lett, 2015, 12: 2056–2060

13 Liu C, Li H C, Sun X, et al. $\mathcal{H}$ distribution for multilook polarimetric SAR data. IEEE Geosci Remote Sens Lett, 2017, 14: 489–493
14 Marino A, Cloude S R, Woodhouse I H. Detecting depolarized targets using a new geometrical perturbation filter. IEEE Trans Geosci Remote Sens, 2012, 50: 3787–3799
15 Novak L M, Sechtin M B, Cardullo M J. Studies of target detection algorithms that use polarimetric radar data. IEEE Trans Aerosp Electron Syst, 1989, 25: 150–165
16 Novak L M, Burl M C. Optimal speckle reduction in polarimetric SAR imagery. IEEE Trans Aerosp Electron Syst, 1990, 26: 293–305
17 Novak L M, Burl M C, Irving W W, et al. Optimal polarimetric processing for enhanced target detection. In: Proceedings of Telesystems Conference Proceedings, 1991. 69–75
18 Liu G, Huang S, Torre A, et al. The multilook polarimetric whitening filter (MPWF) for intensity speckle reduction in polarimetric SAR images. IEEE Trans Geosci Remote Sens, 1998, 36: 1016–1020
19 Liu T, Zhang J, Gao G, et al. CFAR ship detection in polarimetric synthetic aperture radar images based on whitening filter. IEEE Trans Geosci Remote Sens, 2020, 58: 58–81
20 Khan S, Guida R. On fractional moments of multilook polarimetric whitening filter for polarimetric SAR data. IEEE Trans Geosci Remote Sens, 2014, 52: 3502–3512
21 Goodman N R. Statistical analysis based on a certain multivariate complex gaussian distribution (an introduction). Ann Math Statist, 1963, 34: 152–177
22 Mathai A, Saxena R, Haubold H. The H-function: Theory and Applications. New York: Springer, 2010
23 Soulimani A, Benjillali M, Chergui H, et al. On multihop Weibull-fading communications: performance analysis framework and applications. 2016. ArXiv: 1610.08535
24 Paes R L, Lorenzzetti J A, Gherardi D F M. Ship detection using TerraSAR-X images in the Campos Basin (Brazil). IEEE Geosci Remote Sens Lett, 2010, 7: 545–548
25 Ester M. A density-based algorithm for discover erring clusters in large spatial databases with noise. In: Proceedings of the 2nd International Conference on Know ledge Discovery and Data Mining, 1996
26 Krylov V A, Moser G, Serpico S B, et al. On the method of logarithmic cumulants for parametric probability density function estimation. IEEE Trans Image Process, 2013, 22: 3791–3806
27 Nicolas J M. Introduction aux statistiques de deuxème espèce: applications des logs-moments et des logs-cumulants àl'analyse des lois d'images radar. Traitement du Signal (in french), 2002, 19: 139–167
28 Anfinsen S N, Doulgeris A P, Eltoft T. Estimation of the equivalent number of looks in polarimetric synthetic aperture radar imagery. IEEE Trans Geosci Remote Sens, 2009, 47: 3795–3809
29 Anfinsen S N, Doulgeris A P, Eltoft T. Goodness-of-fit tests for multilook polarimetric radar data based on the mellin transform. IEEE Trans Geosci Remote Sens, 2011, 49: 2764–2781
30 Liu T, Cui H-G, Xi Z-M, et al. On log-cumulants of multilook polarimetric whitening filter for polarimetric SAR data. IET Radar Sonar Navigation, 2016, 10: 655–662
31 Wei J J, Li P X, Yang J, et al. A new automatic ship detection method using L-Band polarimetric SAR imagery. IEEE J Sel Top Appl Earth Observations Remote Sens, 2014, 7: 1383–1393
32 Anfinsen S N, Eltoft T. Application of the matrix-variate Mellin transform to analysis of polarimetric radar images. IEEE Trans Geosci Remote Sens, 2011, 49: 2281–2295
33 Kullback S, Leibler R A. On information and sufficiency. Ann Math Statist, 1951, 22: 79–86
34 Liu C, Gierull C H. A new application for PolSAR imagery in the field of moving target indication/ship detection. IEEE Trans Geosci Remote Sens, 2007, 45: 3426–3436

Appendix A

Two approximations have been proposed to simplify the calculation of the PDF of quadratic forms[1]. We can extend the results of the real case to the complex case via the method in the web[2]. The principle of the extension lies on the fact that the real part and the imaginary part of a complex are independent and the results for a complex are just doubling the dimension of a real. Therefore the extended theorem is as follows.

Theorem 1. Let $\boldsymbol{x} \sim N_{\mathrm{d}}(0, \boldsymbol{\Sigma})$ be a d-variate Gaussian random variable with complex positive definite Hermitian covariance matrix $\boldsymbol{\Sigma}$, and $z = \boldsymbol{x}^{\mathrm{H}}\boldsymbol{G}\boldsymbol{x}$ is a quadratic form in $\boldsymbol{x}$. The matrix $\boldsymbol{G}$ is nonnegative definite. Let the rank of $\boldsymbol{G}$ be d and the nonzero eigenvalues of $\boldsymbol{G\Sigma}$ be $\lambda_1, \lambda_2, \ldots, \lambda_{\mathrm{d}}$. The approximating distribution of T can then be

$$z \sim a\chi^2_{2b}/2a \qquad \text{or} \qquad bz \sim c\chi^2_{2d}/2, \tag{A.1}$$

where $c = \sum_{i=1}^{d} \lambda_i / d$, $a = \frac{\sum_{i=1}^{d} \lambda_i^2}{\sum_{i=1}^{d} \lambda_i}$, $b = \frac{\left(\sum_{i=1}^{d} \lambda_i\right)^2}{\sum_{i=1}^{d} \lambda_i^2}$ and H is the superscript of the conjugate transpose. The related parameters can be estimated as follows:

$$\hat{a} = \mathrm{tr}\left[\left(\boldsymbol{G}\hat{\boldsymbol{\Sigma}}\right)^2\right] / \mathrm{tr}\left(\boldsymbol{G}\hat{\boldsymbol{\Sigma}}\right), \tag{A.2-1}$$

$$\hat{b} = \left[\mathrm{tr}\left(\boldsymbol{G}\hat{\boldsymbol{\Sigma}}\right)\right]^2 / \mathrm{tr}\left[\left(\boldsymbol{G}\hat{\boldsymbol{\Sigma}}\right)^2\right], \tag{A.2-2}$$

$$\hat{c} = \mathrm{tr}\left(\boldsymbol{G}\hat{\boldsymbol{\Sigma}}\right) / d, \tag{A.2-3}$$

where $\hat{\boldsymbol{\Sigma}} = \hat{\boldsymbol{\Sigma}}_C$ or $\hat{\boldsymbol{\Sigma}} = \hat{\boldsymbol{\Sigma}}_T$.

The above theorem is the foundation of our following derivations. $z \sim a\chi^2_{2b}/2$ is equivalent to $z \sim \gamma(b, a)$. Here, $\gamma(\alpha, \beta)$ is the Gamma distribution, which can be expressed as

$$\gamma(\alpha, \beta) = \frac{1}{\Gamma(\alpha)} \frac{1}{\beta} \left(\frac{x}{\beta}\right)^{\alpha - 1} \mathrm{e}^{-\frac{x}{\beta}}, \tag{A.3}$$

1) Yuan K H, Bentler P M. Two simple approximations to the distributions of quadratic forms. Brit J Math Stat Psy, 2011, 63: 273–291.

2) Giri N. On the complex analogues of T2- and R2-tests. Ann Math Stat, 1965, 36: 664–670.

where α is the shape parameter, and β is the scale parameter.

In the multilook case, the sum of the independent Gamma distributed variables is distributed as follows, according to the characteristics of the Gamma distribution[3]):

$$z_S = \sum_{i=1}^{L} T_i \sim \gamma\left(Lb, a\right), \tag{A.4}$$

where L is the number of looks.

Therefore, according to the characteristics of the Gamma distribution, the distribution of the average of the sum is

$$z_L = z_S/L \sim \gamma\left(Lb, \frac{a}{L}\right). \tag{A.5}$$

If the detection threshold is assumed to be T, the PFA or PD can be determined as

$$P_{fa/d} = \int_T^{\infty} \gamma\left(Lb, \frac{a}{L}\right) \mathrm{d}z = 1 - \Gamma\left[Lb, \frac{LT}{a}\right], \tag{A.6}$$

where $P_{\rm fa}$ is the PFA, $P_{\rm d}$ is the PD, and L is the number of looks. When $P_{\rm fa}$ is calculated, $\hat{\boldsymbol{\Sigma}} = \hat{\boldsymbol{\Sigma}}_C$, and when $P_{\rm d}$ is calculated, $\hat{\boldsymbol{\Sigma}} = \hat{\boldsymbol{\Sigma}}_T$. If the texture is not a constant, the integration should be used to derive the PFA.

If the texture is GGD-distributed, PFA/PD should be calculated by integrating the texture variable, that is

$$\begin{aligned} P_{fa/d} &= \int_0^{+\infty} \int_T^{+\infty} \gamma\left(Lb, \frac{\tilde{\tau} a}{L}\right) \mathrm{d}z \frac{|v|\, k^k}{\sigma \Gamma(k)} \left(\frac{\tilde{\tau}}{\sigma}\right)^{kv-1} \exp\left\{-k\left(\frac{\tilde{\tau}}{\sigma}\right)^{v}\right\} \mathrm{d}\tilde{\tau} \\ &= \int_T^{+\infty} \gamma\left(Lb, \frac{\tilde{\tau} a}{L}\right) \int_0^{+\infty} \frac{|v|\, k^k}{\sigma \Gamma(k)} \left(\frac{\tilde{\tau}}{\sigma}\right)^{kv-1} \exp\left\{-k\left(\frac{\tilde{\tau}}{\sigma}\right)^{v}\right\} \mathrm{d}\tilde{\tau} \mathrm{d}z \\ &= \frac{1}{\Gamma(Lb)} \frac{|v|\, k^k}{\sigma^{kv}\Gamma(k)} \int_T^{+\infty} \frac{1}{z}\left(\frac{Lz}{a}\right)^{Lb} \int_0^{+\infty} \tilde{\tau}^{-Lb+kv-1} \exp\left\{-\left(\frac{k^{1/v}\tilde{\tau}}{\sigma}\right)^{v} - \frac{Lz}{a}\frac{1}{\tilde{\tau}}\right\} \mathrm{d}\tilde{\tau}\mathrm{d}z. \end{aligned} \tag{A.7}$$

Instituting $x = \frac{k^{1/v}\tilde{\tau}}{\sigma}$, we can obtain the following expression via the definition of the Fox H-function:

$$\begin{aligned} P_{fa/d} &= \frac{1}{\Gamma(L\beta)} \frac{1}{\Gamma(k)} \left(\frac{\sigma}{k^{1/v}}\right)^{-Lb} \int_T^{+\infty} \frac{1}{z}\left(\frac{Lz}{a}\right)^{Lb} |v| \int_0^{+\infty} x^{kv-Lb-1} \exp\left\{-x^{v} - \frac{k^{1/v}Lz}{a\sigma}\frac{1}{x}\right\} \mathrm{d}\tilde{\tau}\mathrm{d}z \\ &= \frac{1}{\Gamma(Lb)} \frac{1}{\Gamma(k)} \frac{k^{1/v}L}{a\sigma} \begin{cases} \int_T^{+\infty} \left(\frac{k^{1/v}Lz}{a\sigma}\right)^{Lb-1} H_{0,2}^{2,0}\left[\frac{k^{1/v}Lz}{a\sigma} \middle| \begin{matrix} \\ (0,1), (\frac{kv-Lb}{v}, \frac{1}{v}) \end{matrix}\right] \mathrm{d}z, & v > 0, \\ \int_T^{+\infty} \left(\frac{k^{1/v}Lz}{a\sigma}\right)^{Lb-1} H_{1,1}^{1,1}\left[\frac{k^{1/v}Lz}{a\sigma} \middle| \begin{matrix} (1-\frac{kv-Lb}{v}, -\frac{1}{v}) \\ (0,1) \end{matrix}\right] \mathrm{d}z, & v < 0. \end{cases} \end{aligned} \tag{A.8}$$

Via the relation equation in [22], we have

$$z^{\sigma} H_{p,q}^{m,n}\left[z \middle| \begin{matrix} (a_p, A_p) \\ (b_q, B_q) \end{matrix}\right] = H_{p,q}^{m,n}\left[z \middle| \begin{matrix} (a_p + \sigma A_p, A_p) \\ (b_q + \sigma B_p, B_q) \end{matrix}\right]. \tag{A.9}$$

The following expression can then be derived:

$$P_{fa/d} = \frac{1}{\Gamma(Lb)} \frac{1}{\Gamma(k)} \frac{k^{1/v}L}{a\sigma} \begin{cases} \int_{\frac{k^{1/v}LT}{a\sigma}}^{+\infty} H_{0,2}^{2,0}\left[y \middle| \begin{matrix} \\ (Lb-1,1), (\frac{kv-1}{v}, \frac{1}{v}) \end{matrix}\right] \mathrm{d}y, & v > 0, \\ \int_{\frac{k^{1/v}LT}{a\sigma}}^{+\infty} H_{1,1}^{1,1}\left[y \middle| \begin{matrix} (1-k+\frac{1}{v}, -\frac{1}{v}) \\ (Lb-1,1) \end{matrix}\right] \mathrm{d}y, & v < 0. \end{cases} \tag{A.10}$$

Via the integration equation in [22], we have

$$\int_0^t x^{\rho-1}(t-x)^{\sigma-1} H_{p,q}^{m,n}\left[bx^k \middle| \begin{matrix} (a_p, A_p) \\ (b_q, B_q) \end{matrix}\right] \mathrm{d}x = t^{\rho+\sigma-1}\Gamma(\sigma) H_{p+1,q+1}^{m,n+1}\left[bt^k \middle| \begin{matrix} (1-\rho,k), (a_p, A_p) \\ (b_q, B_q), (1-\rho-\sigma, k) \end{matrix}\right], \tag{A.11}$$

and we can obtain

$$P_{fa/d} = 1 - \frac{T}{\Gamma(Lb)\Gamma(k)} \left(\frac{k^{1/v}L}{a\sigma}\right) \begin{cases} H_{1,3}^{2,1}\left[\frac{k^{1/v}LT}{a\sigma} \middle| \begin{matrix} (0,1) \\ (Lb-1,1), (\frac{kv-1}{v}, \frac{1}{v}), (-1,1) \end{matrix}\right], & v > 0, \\ H_{2,2}^{1,2}\left[\frac{k^{1/v}LT}{a\sigma} \middle| \begin{matrix} (0,1), (1-k+\frac{1}{v}, -\frac{1}{v}) \\ (Lb-1,1), (-1,1) \end{matrix}\right], & v < 0. \end{cases} \tag{A.12}$$

Supporting information Appendix A. The supporting information is available online at info.scichina.com and link.springer.com. The supporting materials are published as submitted, without typesetting or editing. The responsibility for scientific accuracy and content remains entirely with the authors.

3) Forbes C, Evans M, Hastings N, et al. Statistical Distributions. 4th ed. Wiley: Hoboken, 2010.